Surface phonon-polariton enhanced optical forces in silicon carbide nanostructures

Dongfang Li,[1,2] Nabil M. Lawandy,[1,2,3] and Rashid Zia[1,2,*]

[1]*School of Engineering, Brown University, Box D, Providence, Rhode Island 02912, USA*
[2]*Department of Physics, Brown University, Box 1843, Providence, Rhode Island 02912, USA*
[3]*Spectra Systems Corporation, 321 South Main St, Suite 102, Providence, Rhode Island 02903, USA*
[*]*Rashid_Zia@brown.edu*

Abstract: The enhanced optical forces induced by surface phonon-polariton (SPhP) modes are investigated in different silicon carbide (SiC) nanostructures. Specifically, we calculate optical forces using the Maxwell stress tensor for three different geometries: spherical particles, slab waveguides, and rectangular waveguides. We show that SPhP modes in SiC can produce very large forces, more than one order of magnitude larger than the surface plasmon-polariton (SPP) forces in analogous metal nanostructures. The material and geometric basis for these large optical forces are examined in terms of dispersive permittivity, separation distance, and operating wavelength.

OCIS codes: (350.4855) Optical tweezers or optical manipulation; (220.4880) Optomechanics; (230.7370) Waveguides; (240.5420) Polaritons; (240.6680) Surface plasmons; (240.6690) Surface waves.

References and links

1. D. Van Thourhout and J. Roels, "Optomechanical device actuation through the optical gradient force," Nat. Photonics **4**(4), 211–217 (2010).
2. J. Ma and M. L. Povinelli, "Applications of optomechanical effects for on-chip manipulation of light signals," Curr. Opin. Solid State Mater. Sci. **16**(2), 82–90 (2012).
3. M. L. Povinelli, M. Loncar, M. Ibanescu, E. J. Smythe, S. G. Johnson, F. Capasso, and J. D. Joannopoulos, "Evanescent-wave bonding between optical waveguides," Opt. Lett. **30**(22), 3042–3044 (2005).
4. M. Li, W. H. P. Pernice, C. Xiong, T. Baehr-Jones, M. Hochberg, and H. X. Tang, "Harnessing optical forces in integrated photonic circuits," Nature **456**(7221), 480–484 (2008).
5. F. Riboli, A. Recati, M. Antezza, and I. Carusotto, "Radiation induced force between two planar waveguides," Eur. Phys. J. D **46**(1), 157–164 (2008).
6. M. Li, W. H. P. Pernice, and H. X. Tang, "Tunable bipolar optical interactions between guided lightwaves," Nat. Photonics **3**(8), 464–468 (2009).
7. L. Novotny, R. X. Bian, and X. S. Xie, "Theory of nanometric optical tweezers," Phys. Rev. Lett. **79**(4), 645–648 (1997).
8. J. R. Arias-González and M. Nieto-Vesperinas, "Optical forces on small particles: attractive and repulsive nature and plasmon-resonance conditions," J. Opt. Soc. Am. A **20**(7), 1201–1209 (2003).
9. A. J. Hallock, P. L. Redmond, and L. E. Brus, "Optical forces between metallic particles," Proc. Natl. Acad. Sci. U.S.A. **102**(5), 1280–1284 (2005).
10. R. Quidant, D. Petrov, and G. Badenes, "Radiation forces on a Rayleigh dielectric sphere in a patterned optical near field," Opt. Lett. **30**(9), 1009–1011 (2005).
11. É. Lamothe, G. Lévêque, and O. J. F. Martin, "Optical forces in coupled plasmonic nanosystems: near field and far field interaction regimes," Opt. Express **15**(15), 9631–9644 (2007).
12. B. Sepúlveda, J. Alegret, and M. Käll, "Nanometric control of the distance between plasmonic nanoparticles using optical forces," Opt. Express **15**(22), 14914–14920 (2007).
13. A. S. Zelenina, R. Quidant, and M. Nieto-Vesperinas, "Enhanced optical forces between coupled resonant metal nanoparticles," Opt. Lett. **32**(9), 1156–1158 (2007).
14. P. Chu and D. L. Mills, "Laser-induced forces in metallic nanosystems: the role of plasmon resonances," Phys. Rev. Lett. **99**(12), 127401 (2007).
15. P. Chu and D. L. Mills, "Electromagnetic response of nanosphere pairs: collective plasmon resonances, enhanced fields, and laser-induced forces," Phys. Rev. B **77**(4), 045416 (2008).
16. P. Chu and D. L. Mills, "Laser-induced forces in metallic nanosystems: the role of plasmon resonances," Phys. Rev. Lett. **99**(12), 127401 (2007).
17. L. Huang and O. J. F. Martin, "Reversal of the optical force in a plasmonic trap," Opt. Lett. **33**(24), 3001–3003 (2008).

#187913 - $15.00 USD Received 26 Jun 2013; revised 15 Aug 2013; accepted 16 Aug 2013; published 30 Aug 2013

18. J. Ng, R. Tang, and C. T. Chan, "Electrodynamics study of plasmonic bonding and antibonding forces in a bisphere," Phys. Rev. B **77**(19), 195407 (2008).
19. D. Woolf, M. Loncar, and F. Capasso, "The forces from coupled surface plasmon polaritons in planar waveguides," Opt. Express **17**(22), 19996–20011 (2009).
20. C. G. Huang and L. Zhu, "Enhanced optical forces in 2D hybrid and plasmonic waveguides," Opt. Lett. **35**(10), 1563–1565 (2010).
21. A. Bonakdar, J. Kohoutek, D. Dey, and H. Mohseni, "Optomechanical nanoantenna," Opt. Lett. **37**(15), 3258–3260 (2012).
22. V. Garcés-Chávez, R. Quidant, P. J. Reece, G. Badenes, L. Torner, and K. Dholakia, "Extended organization of colloidal microparticles by surface plasmon polariton excitation," Phys. Rev. B **73**(8), 085417 (2006).
23. G. Volpe, R. Quidant, G. Badenes, and D. Petrov, "Surface plasmon radiation forces," Phys. Rev. Lett. **96**(23), 238101 (2006).
24. M. Righini, A. S. Zelenina, C. Girard, and R. Quidant, "Parallel and selective trapping in a patterned plasmonic landscape," Nat. Phys. **3**(7), 477–480 (2007).
25. A. N. Grigorenko, N. W. Roberts, M. R. Dickinson, and Y. Zhang, "Nanometric optical tweezers based on nanostructured substrates," Nat. Photonics **2**(6), 365–370 (2008).
26. M. Righini, G. Volpe, C. Girard, D. Petrov, and R. Quidant, "Surface plasmon optical tweezers: tunable Optical Manipulation in the Femtonewton Range," Phys. Rev. Lett. **100**(18), 186804 (2008).
27. K. Wang, E. Schonbrun, and K. B. Crozier, "Propulsion of gold nanoparticles with surface plasmon polaritons: evidence of enhanced optical force from near-field coupling between gold particle and gold film," Nano Lett. **9**(7), 2623–2629 (2009).
28. K. Wang, E. Schonbrun, P. Steinvurzel, and K. B. Crozier, "Scannable plasmonic trapping using a gold stripe," Nano Lett. **10**(9), 3506–3511 (2010).
29. M. L. Juan, M. Righini, and R. Quidant, "Plasmon nano-optical tweezers," Nat. Photonics **5**(6), 349–356 (2011).
30. J. Kohoutek, D. Dey, A. Bonakdar, R. Gelfand, A. Sklar, O. G. Memis, and H. Mohseni, "Opto-mechanical force mapping of deep subwavelength plasmonic modes," Nano Lett. **11**(8), 3378–3382 (2011).
31. K. Wang, E. Schonbrun, P. Steinvurzel, and K. B. Crozier, "Trapping and rotating nanoparticles using a plasmonic nano-tweezer with an integrated heat sink," Nat. Commun. **2**, 469 (2011).
32. M. F. Ashby, *Materials Selection in Mechanical Design* (Butterworth-Heinemann, 2005).
33. Y. T. Yang, K. L. Ekinci, X. M. H. Huang, L. M. Schiavone, M. L. Roukes, C. A. Zorman, and M. Mehregany, "Monocrystalline silicon carbide nanoelectromechanical systems," Appl. Phys. Lett. **78**(2), 162–164 (2001).
34. X. M. Henry Huang, C. A. Zorman, M. Mehregany, and M. L. Roukes, "Nanoelectromechanical systems: nanodevice motion at microwave frequencies," Nature **421**(6922), 496–496 (2003).
35. S. C. Jun, J. H. Cho, W. K. Kim, Y. M. Jung, S. Hwang, S. Shin, J. Y. Kang, J. Shin, I. Song, J. Y. Choi, S. Lee, and J. M. Kim, "Resonance properties of 3C-SiC nanoelectromechanical resonator in room-temperature magnetomotive transduction," IEEE Electron Device Lett. **30**(10), 1042–1044 (2009).
36. H. Mutschke, A. C. Andersen, D. Clement, T. Henning, and G. Peiter, "Infrared properties of SiC particles," Astron. Astrophys. **345**, 187–202 (1999).
37. R. Hillenbrand, T. Taubner, and F. Keilmann, "Phonon-enhanced light matter interaction at the nanometre scale," Nature **418**(6894), 159–162 (2002).
38. T. Taubner, D. Korobkin, Y. Urzhumov, G. Shvets, and R. Hillenbrand, "Near-field microscopy through a SiC superlens," Science **313**(5793), 1595–1595 (2006).
39. J. J. Greffet, R. Carminati, K. Joulain, J. P. Mulet, S. P. Mainguy, and Y. Chen, "Coherent emission of light by thermal sources," Nature **416**(6876), 61–64 (2002).
40. Y. De Wilde, F. Formanek, R. Carminati, B. Gralak, P. A. Lemoine, K. Joulain, J. P. Mulet, Y. Chen, and J. J. Greffet, "Thermal radiation scanning tunnelling microscopy," Nature **444**(7120), 740–743 (2006).
41. J. A. Schuller, T. Taubner, and M. L. Brongersma, "Optical antenna thermal emitters," Nat. Photonics **3**(11), 658–661 (2009).
42. J. A. Schuller, R. Zia, T. Taubner, and M. L. Brongersma, "Dielectric metamaterials based on electric and magnetic resonances of silicon carbide particles," Phys. Rev. Lett. **99**(10), 107401 (2007).
43. A. D. Rakic, A. B. Djurisic, J. M. Elazar, and M. L. Majewski, "Optical properties of metallic films for vertical-cavity optoelectronic devices," Appl. Opt. **37**(22), 5271–5283 (1998).
44. P. K. Aravind, A. Nitzan, and H. Metiu, "The interaction between electromagnetic resonances and its role in spectroscopic studies of molecules adsorbed on colloidal particles or metal spheres," Surf. Sci. **110**(1), 189–204 (1981).
45. L. Novotny and B. Hecht, *Principles of Nano-Optics* (Cambridge University Press, 2006).
46. P. Lusse, P. Stuwe, J. Schule, and H. G. Unger, "Analysis of vectorial mode fields in optical waveguides by a new finite-difference method," J. Lightwave Technol. **12**(3), 487–494 (1994).
47. R. D. Kekatpure, A. C. Hryciw, E. S. Barnard, and M. L. Brongersma, "Solving dielectric and plasmonic waveguide dispersion relations on a pocket calculator," Opt. Express **17**(26), 24112–24129 (2009).
48. X. D. Yang, Y. M. Liu, R. F. Oulton, X. B. Yin, and X. A. Zhang, "Optical forces in hybrid plasmonic waveguides," Nano Lett. **11**(2), 321–328 (2011).
49. H. Li, J. W. Noh, Y. Chen, and M. Li, "Enhanced optical forces in integrated hybrid plasmonic waveguides," Opt. Express **21**(10), 11839–11851 (2013).

#187913 - $15.00 USD Received 26 Jun 2013; revised 15 Aug 2013; accepted 16 Aug 2013; published 30 Aug 2013

1. Introduction

Optomechanical devices [1, 2], especially those leveraging the optical forces produced by guide modes in photonic waveguides [3–6], have attracted great interest. In this context, the surface plasmon-polariton (SPP) enhanced optical forces in metal nanostructures have been thoroughly investigated in both theoretical [7–21] and experimental [22–31] studies. (For a detailed review of surface plasmon forces in the context of optical tweezers, see [29].) Similar to SPP modes supported by metals, polar dielectrics support surface phonon-polariton (SPhP) modes that can be used to guide and concentrate intense electromagnetic energy, creating a strong enhancement of optical forces. The investigation of SPhP enhanced optical forces may allow the extension of optomechanical devices into new material systems and frequency regimes.

For example, silicon carbide (SiC) materials are widely used for their exceptional electronic, mechanical, and thermal properties. SiC is an important semiconductor with a large band gap and high thermal conductivity. Given its high Young's modulus to density ratio [32], SiC is an ideal material for high frequency mechanical resonators, and it has been explored for applications in nano-electro-mechanical systems (NEMS) [33–35]. SiC also exhibits unique optical properties that may make it ideally suited for optomechanical devices. As a polar dielectric, SiC supports strong SPhP resonances in the infrared region around 11 μm [36]. These resonances have been the topic of considerable study in the near-field and nano-optics community for applications in high-resolution infrared microscopy [37, 38], coherent thermal emission [39], thermal radiation microscopy [40], thermal optical antennas [41], and dielectric metamaterials [42]. Compared to flexible and lossy metals, SiC has a considerably higher Young's modulus and lower optical damping constant. The longer wavelength SPhPs in SiC can also induce stronger coupling and larger optical forces for similarly sized structures.

To highlight the similarities and differences between the optical properties of SiC and metallic materials, the plots in Figs. 1(a) and 1(b) show the complex permittivity for SiC and gold (Au). In particular, we plot the frequency-dependent relative permittivity $\varepsilon_r(\omega)$ of 6H-SiC in the direction perpendicular to the principal axis [36] around 11 μm, and we compare this to the relative permittivity of Au in the visible range [43]. (For simplicity throughout this paper, we model SiC as an isotropic material with the complex permittivity shown here and, therefore, neglect the minor variations in SiC optical properties due to polytype and orientation.) Note that the real parts of the relative permittivity $\mathrm{Re}\{\varepsilon_r(\omega)\}$ for Au and SiC are comparable over these two different spectral regimes. However, the imaginary part $\mathrm{Im}\{\varepsilon_r(\omega)\}$ of SiC is significantly smaller than that of Au. This suggests that SiC nanostructures can support infrared SPhP modes that are very similar to the visible SPP modes of Au nanostructures, but with substantially lower optical losses.

#187913 - $15.00 USD Received 26 Jun 2013; revised 15 Aug 2013; accepted 16 Aug 2013; published 30 Aug 2013

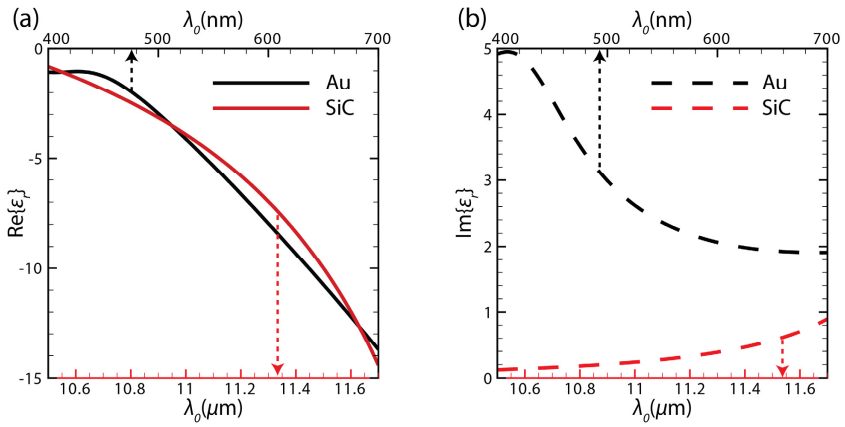

Fig. 1. Comparison of the (a) real and (b) imaginary parts of the relative permittivity for Au in visible range and 6H-SiC in the direction perpendicular to the principal axis around 11 μm.

In this paper, we examine the optical forces arising from SiC SPhP modes and Au SPP modes in three different geometries. First, under the quasistatic approximation, we calculate the optical forces between two spherical particles and investigate the effect of the complex permittivity. Next, the optical forces between two slab waveguides are simulated, from which the effect of the operating wavelength is studied and an approximate analytical explanation is derived. Finally, we calculate the optical forces in a more practical structure consisting of two free standing rectangular waveguides. Our simulation results show that the optical forces in SiC nanostructures are more than one order of magnitude stronger than those in similar Au nanostructures.

2. Simulation methods and results

2.1 Attractive optical forces between two spherical particles

First, we investigate the optical force between two spherical particles with identical radius r_0 = 30 nm in an external electric field $\vec{E} = E_0 e^{i\omega t}\hat{z}$. As shown in the inset of Fig. 2(a), the two spheres are placed in free space a distance *2d* apart from each other along the *z*-axis such that there is a small gap width ($w = 2d - 2r_0$) between them.

We consider the case where the sphere radius is much smaller than the operating wavelength ($r_0 \ll \lambda_0$), whereby retardation effects can be neglected and the problem becomes quasistatic. In this scenario, the two spheres will be polarized along the *z*-axis due to the displacement in opposite directions of positively-charged Si and negatively-charged C sites, inducing an attractive force between the two spheres.

In the quasistatic limit, the Helmholtz wave equation reduces to Laplace's equation. Following the method used by Aravind *et al.* [44], a general solution to Laplace's equation can be obtained by separation of variables for the two-particle system in bispherical coordinates (μ, η, φ). In this coordinate system, the constant $\mu_0 = \pm \sin h^{-1}(\sqrt{d^2 - r_0^2}/r_0)$ defines spherical shells with radius r_0 centered a distance d from the origin along the *z*-axis. Using the Maxwell stress tensor (MST), the force expression can be written as [9]:

$$\vec{F} = \oint \langle \vec{\vec{T}} \rangle \cdot d\vec{S} = \hat{z}\varepsilon_0 \pi \int_0^{\pi} \frac{\sin(\eta)\left(\cos h(\mu_0)\cos(\eta) - 1\right)}{4\left(\cos h(\mu_0) - \cos(\eta)\right)^2} \left(\sum_{n=0}^{n_{\max}} X_n \sum_{m=0}^{m_{\max}} X_m^{*} \right) d\eta. \qquad (1)$$

#187913 - $15.00 USD Received 26 Jun 2013; revised 15 Aug 2013; accepted 16 Aug 2013; published 30 Aug 2013

$$X_n = e^{(n+\frac{1}{2})\mu_0} A_n^0 \left[(2n+1)\left(\cos(\eta) - \cosh(\mu_0)\right) - \sinh(\mu_0) \right]$$
$$+ e^{-(n+\frac{1}{2})\mu_0} \left[2cE_0\sqrt{2\pi(2n+1)} + A_n^0 \right] \left[(2n+1)\left(\cos(\eta) - \cosh(\mu_0)\right) + \sinh(\mu_0) \right], \quad (2)$$

where $\vec{T}$ is the MST, $\bar{S}$ is the surface of the sphere defined by μ_0, A_n^0 are the expansion coefficients in the potential expression of the surrounding environment $\phi = -E_0 z + \sqrt{\cosh(\mu) - \cos(\eta)} \sum_{n=0}^{\infty} [A_n^0 e^{(n+1/2)\mu} - A_n^0 e^{-(n+1/2)\mu}] Y_n^0(\eta, \varphi)$, ε_0 is the vacuum permittivity, and n_{max} and m_{max} are the cutoff numbers for the respective summations. Here, we use $n_{max} = m_{max} = 40$, which is sufficient to confirm convergence of the summations.

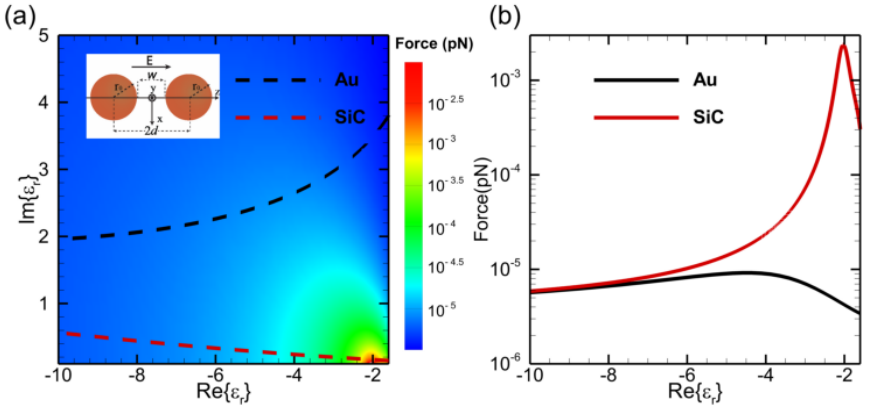

Fig. 2. (a) Magnitude of the attractive optical forces versus relative permittivity for a fixed gap width of 100 nm, r_0 = 30 nm, and incident power intensity of 1 kW/cm^2. The inset shows a sketch of the two spherical particles system. Dashed lines show the relative permittivity of Au (black) and SiC (red). (b) Attractive optical forces calculated for two Au and two SiC spheres.

Due to the quasistatic approximation, the operating wavelength has only an indirect effect through the dispersive relative permittivity. We numerically investigate the effect of the complex permittivity on optical forces in this system. For example, as shown in Fig. 2(a) for a gap width w = 100 nm, we map the optical force versus both real and imaginary parts of relative permittivity in the range from −10 to −1.6 and 0.1 to 5 respectively. Figure 2(a) highlights the $\varepsilon_r(\omega) = -2$ resonance condition for the optical force between two spherical particles in vacuum; this resonance is directly related to the $\varepsilon_{particle} = -2\,\varepsilon_{host}$ surface polariton resonance for spherical particles [45]. (The dipole moment of a spherical particle can be written as: $\vec{p}_{dipole} = 4\pi\varepsilon_{host}\vec{E}_0\, r_0^3 \left(\varepsilon_{particle} - \varepsilon_{host}\right) / \left(\varepsilon_{particle} + 2\varepsilon_{host}\right)$, which exhibits a resonance when the denominator approaches zero.) When either the real or imaginary parts of the relative permittivity stray from the $\varepsilon_r(\omega) = -2$ resonance, the magnitude of the optical force will dramatically decrease. For reference, we plot the relative permittivity of SiC (red dashed line) and Au (black dashed line) in Fig. 2(a) over the wavelength range from 10.66 to 11.5 μm and 465 to 637 nm, respectively. Note that the relative permittivity line of Au is far away from the resonance point, while that of SiC passes near the resonance region. The maximum force can be produced by operating at λ_0 = 10.73 μm, where SiC's relative permittivity $\varepsilon_r(\omega)$ = −2 + 0.16i is very close to the pure resonance condition; however, a similar relative permittivity cannot be obtained for Au at any wavelength. In order to clarify and compare the magnitude of the optical force in this structure for SiC and Au, we extract the optical force along the red and black dashed lines in Fig. 2(a) and plot them in Fig. 2(b). It clearly shows that the maximum optical force for SiC is over two orders magnitude larger than that for Au.

#187913 - $15.00 USD Received 26 Jun 2013; revised 15 Aug 2013; accepted 16 Aug 2013; published 30 Aug 2013

In addition to a fixed gap width, we also investigated the optical forces as a function of varying gap width. These calculations were performed at four different infrared wavelengths for SiC and four corresponding wavelengths for Au, in which $\mathrm{Re}\{\varepsilon_r(\omega)\}$ are equal but $\mathrm{Im}\{\varepsilon_r(\omega)\}$ differs. The inset of Fig. 3 shows that at short gap widths (w < 30 nm) for certain values of relative permittivity with small imaginary parts, the optical force doesn't decrease monotonically as the gap width increases, but rather, exhibits several resonant peaks. This is due to a matching of the relative permittivity and gap width to collective modes [14–16, 18]. However, at large gap widths (w > 30 nm), as the gap width is increased, the interaction between two spheres becomes weaker and the optical forces monotonically decrease. As shown in Fig. 3, the optical forces of SiC (red solid line) and Au (red dashed lines) at $\mathrm{Re}\{\varepsilon_r(\omega)\} = -10$ overlap with each other; when $\mathrm{Re}\{\varepsilon_r(\omega)\}$ is far from the resonance condition, the $\mathrm{Im}\{\varepsilon_r(\omega)\}$ has little effect on optical forces. As $\mathrm{Re}\{\varepsilon_r(\omega)\}$ approaches the $\varepsilon_r(\omega) = -2$ resonance condition though, the $\mathrm{Im}\{\varepsilon_r(\omega)\}$ has a much larger effect. Compared to the optical forces for Au at $\mathrm{Re}\{\varepsilon_r(\omega)\} = -2$ (black dashed line), those for SiC (black solid line) are over two orders stronger. Notably, this large optical force enhancement is also sustained for a large range of gap widths (30-500 nm).

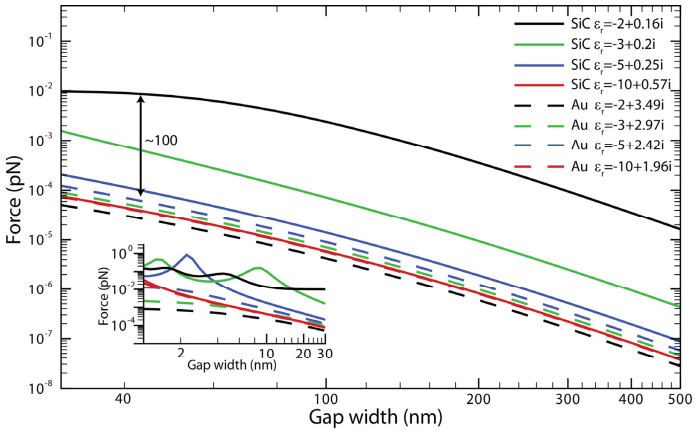

Fig. 3. Optical forces between two identical spherical particles with radius 30 nm versus gap width. Incident power intensity is 1 kW/cm^2. The inset shows the optical forces for small gap widths. Dashed lines show the optical forces calculated for Au particles for illumination wavelengths of 476.5 nm (black), 501 nm (green), 543 nm (blue), and 637 nm (red). Solid lines show the optical forces calculated for SiC particles for illumination wavelengths of 10.73 μm (black), 10.88 μm (green), 11.12 μm (blue), and 11.5 μm (red).

2.2 Optical forces between two slab waveguides

The second structure we consider is composed of two parallel slab waveguides as shown in Fig. 4(a), where d defines the thickness of the slabs and w is half of the gap width between them. SPhPs and SPPs in this structure exist as transverse magnetic (TM) modes propagating along the z-axis. Only H_x, E_y and E_z field components are non-zero and the modes are defined according to the symmetry of the electric field component E_z, with respect to x-z plane, as shown in Figs. 4(b) and 4(c). The wave vector is given by $\bar{k}_i = k_{zi}\hat{z} - ik_{yi}\hat{y}$, where the subscript i = 1 denotes the slabs (SiC or Au) and i = 2 is the surrounding material (air in our calculations). The time averaged optical force $\langle F_y \rangle$ between the two slabs is proportional to T_{yy} component of the MST, which can be written as:

$$T_{yy} = \varepsilon_0 E_y E_y^* - \frac{1}{2}\left[\varepsilon_0\left(E_y E_y^* + E_z E_z^*\right) + \mu_0 H_x H_x^*\right] = \frac{1}{2}\left[\varepsilon_0\left(E_y E_y^* - E_z E_z^*\right) - \mu_0 H_x H_x^*\right]. \quad (3)$$

#187913 - $15.00 USD Received 26 Jun 2013; revised 15 Aug 2013; accepted 16 Aug 2013; published 30 Aug 2013

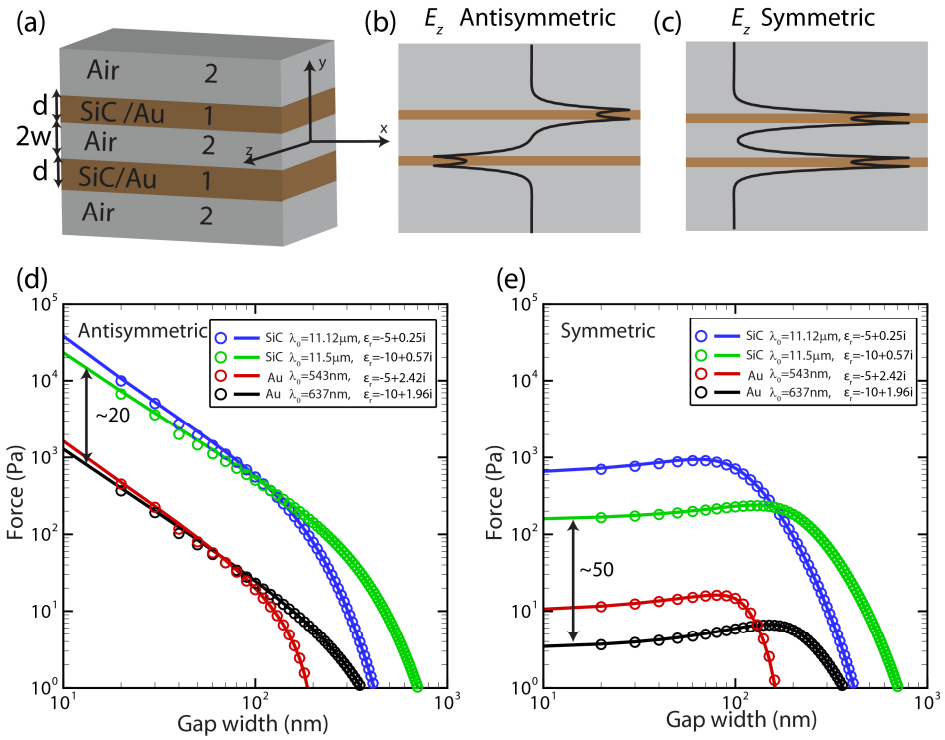

Fig. 4. (a) Sketch of the five-layer, coupled two-slab waveguide system. (b) and (c) show schematic representations of the field profiles for the antisymmetric and symmetric modes. (d) and (e) compare the magnitude of optical forces for SPhPs in SiC and SPPs in Au for the: (d) attractive antisymmetric mode and (e) repulsive symmetric mode. Solid curves are calculated by the iteration method whereas empty circles are the results of FDFD calculation.

Two different methods are applied to obtain field profiles. In the first method, the field profiles are obtained using a vectorial magnetic field finite-difference frequency-domain (FDFD) mode solver [46]. In the second method, we use an iteration technique [47] to solve the complex transcendental dispersion equation for TM modes. For the antisymmetric mode in a five layer system, the dispersion equation is [19]:

$$\frac{k_{y2}\varepsilon_1}{k_{y1}\varepsilon_2}\tanh\left(k_{y2}w\right)=-\frac{\frac{k_{y1}}{\varepsilon_1}\sinh\left(k_{y1}d\right)+\frac{k_{y2}}{\varepsilon_2}\cosh\left(k_{y1}d\right)}{\frac{k_{y1}}{\varepsilon_1}\cosh\left(k_{y1}d\right)+\frac{k_{y2}}{\varepsilon_2}\sinh\left(k_{y1}d\right)}. \tag{4}$$

We selectively choose the following form for the iteration function due to its rapid convergence ($\Delta k_{y2} < 1\ \mathrm{m}^{-1}$ in less than 20 iterations for most data points):

$$k_{y2}=k_{y1}\frac{-\frac{\varepsilon_1}{\varepsilon_2}\left(1+\tanh\left(k_{y2}w\right)\right)+\sqrt{\left[\frac{\varepsilon_1}{\varepsilon_2}\left(1+\tanh\left(k_{y2}w\right)\right)\right]^2-4(\frac{\varepsilon_1}{\varepsilon_2})^2\tanh^2\left(k_{y1}d\right)\tanh\left(k_{y2}w\right)}}{2(\frac{\varepsilon_1}{\varepsilon_2})^2\tanh\left(k_{y1}d\right)\tanh\left(k_{y2}w\right)}. \tag{5}$$

#187913 - $15.00 USD Received 26 Jun 2013; revised 15 Aug 2013; accepted 16 Aug 2013; published 30 Aug 2013

For the symmetric mode, the same procedure is followed with $\coth(k_{y2}w)$ being substituted for $\tanh(k_{y2}w)$ in Eqs. (4) and (5). The field profiles are then calculated following the formalism in [19].

We calculate the optical forces for the attractive antisymmetric and repulsive symmetric modes in SiC and Au operating at wavelengths for which $\mathrm{Re}\{\varepsilon_r(\omega)\} = -5$ and -10. These values of the relatively permittivity are specifically chosen to be far from the resonance condition for a planar surface (i.e. $\mathrm{Re}\{\varepsilon_r(\omega)\} = -1$), so that we can study the effect of optical wavelength and also that the SPP and SPhP modes will have appreciable propagation lengths. The thickness of each slab waveguide in our simulation is 20 nm, and the average value of the power distributed over the x-axis is 1 mW/μm. In Figs. 4(d) and 4(e), the optical forces calculated by the iteration method are shown in solid curves while the FDFD results are plotted by empty circles. Good agreement is achieved between the results of both methods. The behavior of the optical force versus the gap width is consistent with the analysis of Woolf *et al.* [19] for SPP enhanced forces in coupled metallic waveguides. There are two main regimes: for large gap widths, the optical forces in antisymmetric and symmetric modes have nearly equivalent magnitudes; at small gap widths, the magnitude of the attractive force for the antisymmetric mode shows an exponential dependence on gap width, whereas the repulsive force for the symmetric mode is only weakly related to gap width. The distinct behaviors in these two regimes can be understood by the penetration depth $\delta_2 = 1/\mathrm{Re}\{k_{y2}\}$ of the electromagnetic fields into the gap. For a single slab placed in air with thickness d, the dispersion relation for the symmetric mode of this three layer system simplifies to $\tanh(k_{y1}d/2) = -k_{y1}/(\varepsilon_{1r}k_{y2})$. In a sufficiently thin slab $(d < 1/k_{y1})$, the solution to the dispersion relation is $k_{y2} \approx -2/(\varepsilon_{1r}d)$, which corresponds to a penetration depth of $\delta_2 \approx -\mathrm{Re}\{\varepsilon_{1r}\}d/2$. For $w < \delta_2$, strong mode coupling between the two slabs leads to different gap width dependencies for optical forces from the antisymmetric and symmetric modes; while for $w > \delta_2$, the mode coupling becomes weak, and the optical forces in both modes are almost identical in magnitude. Despite the large difference in operating wavelengths for SiC and Au, this simple analysis predicts that the crossover point between the two regimes should occur for similar gap widths, i.e. $2\delta_2$ = 100 (200) nm for $\mathrm{Re}\{\varepsilon_r\} = -5$ (-10), which is consistent with Figs. 4(d) and 4(e).

Compared to the optical forces for Au at wavelengths of 543 nm and 637 nm, the optical forces for SiC with similar real parts of relative permittivity are around 20 (50) times stronger for the antisymmetric (symmetric) modes at small gap widths ($w < \delta_2$). To understand the underlying reason for this enhancement, we analytically investigate the effect of wavelength on the optical forces for both symmetric and antisymmetric modes. In the following analysis, we focus on small gap width structures $w < \delta_2$, where largest forces are seen and which are equivalent to $k_{y2}w < 1$. For long wavelengths, $\lambda_i \gg 2\pi/|k_z|$ where $\lambda_i \equiv \lambda_0/|\sqrt{\varepsilon_{ri}}|$, $k_z \approx k_{y1} \approx k_{y2}$ can be obtained. Furthermore, for a sufficiently small thickness d, we can make the assumption that $k_{y1}d < 1$. Applying the above approximations to Eq. (4) and approximating $\tanh(x) \approx x$, we obtain the following expression for the antisymmetric mode:

$$k_{y2} \approx \frac{-(\frac{\varepsilon_1}{\varepsilon_2}w + d) + \sqrt{(\frac{\varepsilon_1}{\varepsilon_2}w + d)^2 - 4(\frac{\varepsilon_1}{\varepsilon_2})^3 wd}}{2(\frac{\varepsilon_1}{\varepsilon_2})^2 wd}. \tag{6}$$

Similarly, for the symmetric mode under the same assumptions, we obtain:

$$k_{y2} \approx -\frac{\varepsilon_2}{\varepsilon_1 d + \varepsilon_2 w}. \tag{7}$$

#187913 - $15.00 USD Received 26 Jun 2013; revised 15 Aug 2013; accepted 16 Aug 2013; published 30 Aug 2013

Due to the assumption $|k_z| \gg 2\pi/\lambda_i$ and the relation $E_y = -k_z H_x/(\omega\varepsilon)$ derived from Maxwell's equations, we find that $\varepsilon_0 E_y E_y^* / (\mu_0 H_x H_x^*) = |k_z|^2 / k_0^2 >> 1$. Thus, the H_x magnetic field contribution to the optical force can be neglected compared to the E_y contribution, which reduces the MST in Eq. (3) to $T_{yy} \approx \varepsilon_0 (E_y E_y^* - E_z E_z^*)/2$. Equations (6) and (7) show that the wavevector $\bar{k}$ is independent of wavelength under the above assumptions. Interestingly though, both $E_y E_y^*$ and $E_z E_z^*$ are directly proportional to the wavelength, as can be seen from the formalism of Woolf *et al.* in [19]. (Note that the E_y and E_z terms both contain an explicit λ_0 dependence through the frequency ω, as shown in Eqs. (4) and (5) in [19], but there is an additional $1/\sqrt{\lambda_0}$ term from the field amplitude coefficients, see Eq. (13) in [19]. Therefore, $E_y E_y^*$ and $E_z E_z^*$ both scale linearly with λ_0.) From these derivations, we clearly see that the optical force is approximately proportional to the operating wavelength under the assumptions that (i) the penetration depth is larger than the structure size ($w < \delta_2$ and $d < \delta_2$) and (ii) we are operating at long wavelengths ($\lambda_i \gg 2\pi/|k_z|$).

In Figs. 5(a) and 5(b), we consider a hypothetical material with relative permittivity $\varepsilon_r = -10 + 2i$ for a range of wavelengths and compare the magnitude of optical forces calculated by the iteration method (solid lines) and our analytical approximation (empty circles). For long wavelengths, the analytical approximation accurately predicts the optical forces for both the antisymmetric and symmetric cases, and thus, we find that the optical forces do indeed scale linearly with operating wavelength. For small operating wavelengths, the analytical approximation also accurately predicts the forces calculated for the antisymmetric case, but as the wavelength is no longer large enough compared to $2\pi/|k_z|$, the approximation begins to fail and overestimates the forces for the symmetric mode. For completeness, it should also be noted that this approximation fails for both antisymmetric and symmetric modes when the relative permittivity approaches the surface polariton resonance condition ($\varepsilon_r = -1$); for small magnitudes of the relative permittivity (e.g. $\varepsilon_r \approx -2$), minor errors in the approximate $\bar{k}$ vector have a disproportion impact on the predicted forces, and thus the analytical approximation diverges from the iteration result. (Also, for small magnitudes of the relative permittivity, Eq. (6) will no longer be a good approximation for the antisymmetric modes, because $k_{y1}d < 1$ will not be satisfied.)

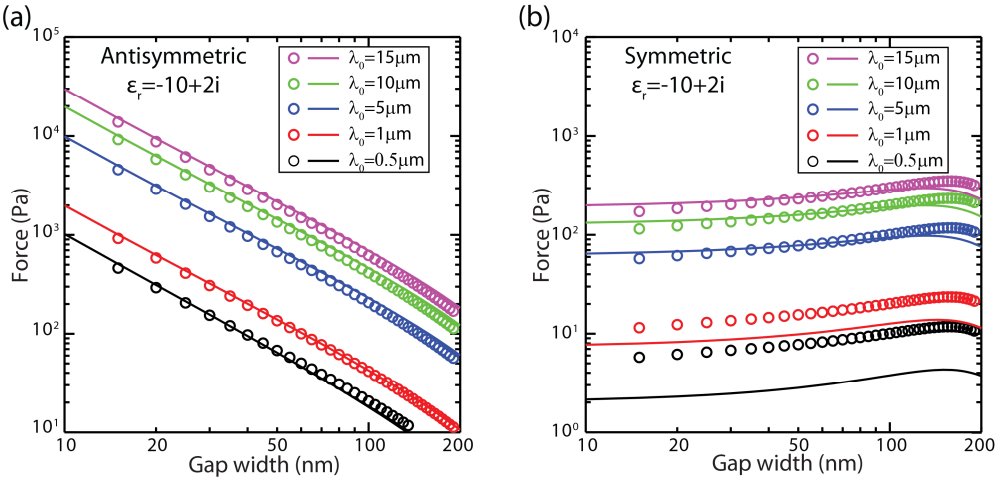

Fig. 5. Magnitude of the optical forces for the (a) attractive antisymmetric mode and (b) repulsive symmetric mode calculated by the iteration method (solid lines) and analytical approximation (empty circles) for a hypothetical material with relative permittivity $\varepsilon_r = -10 + 2i$ at different operating wavelengths.

#187913 - $15.00 USD Received 26 Jun 2013; revised 15 Aug 2013; accepted 16 Aug 2013; published 30 Aug 2013

With the above calculations, we have shown that the optical forces between SiC slab waveguides are more than one order of magnitude larger than those for Au slab waveguides. Furthermore, we have derived a simple analytical approximation that illustrates how this optical force enhancement can be directly attributed to the increased operating wavelength for SiC. Accordingly, the observed 20-50 fold enhancements shown in Fig. 4 are consistent with the ~20 fold increase in operating wavelength from ~500 nm for Au to ~10 μm for SiC.

2.3 Optical forces between two rectangular waveguides

Finally, we investigate the optical forces between two rectangular waveguides, as shown in Fig. 6(a), which represent a more practical geometry for integrated optical circuits. The cross section of each waveguide is set to be 310 nm by 310 nm. We use the same FDFD method [46] discussed in the previous section to solve for the waveguide modes and obtain the field profiles. E_z components of the fundamental antisymmetric and symmetric modes are shown in Figs. 6(b) and 6(c) respectively. Note that the fields in the antisymmetric mode are more confined than those in the symmetric mode, and consequently, the antisymmetric mode exhibits much stronger optical forces. Therefore, in this section, we focus on the optical forces corresponding to the antisymmetric mode, which are attractive in nature.

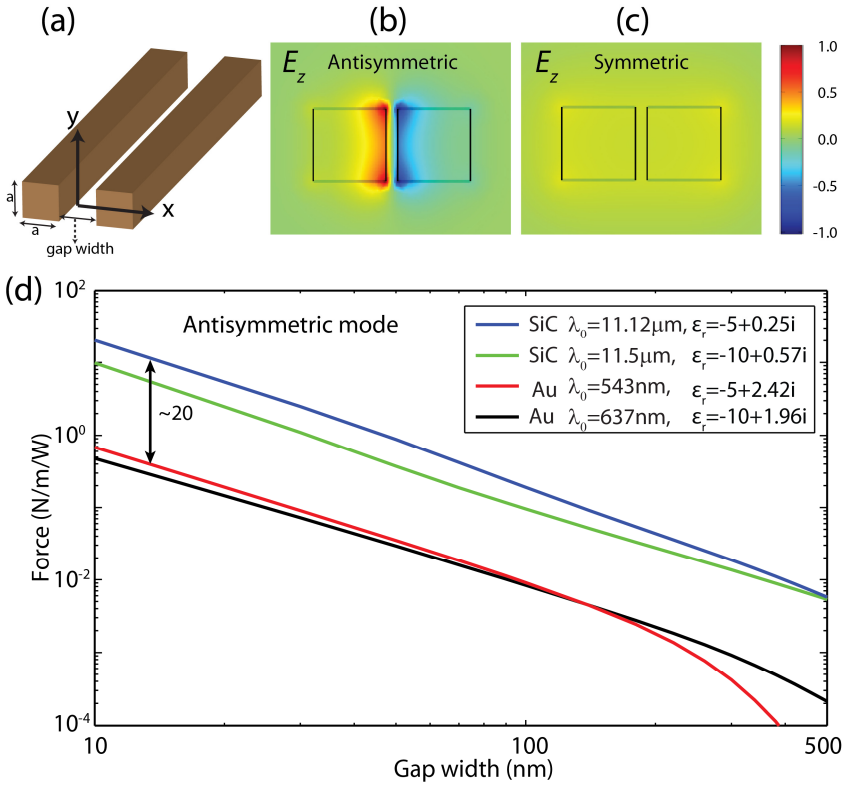

Fig. 6. (a) Sketch of the coupled two rectangular waveguide structure, where each waveguide has a square cross section defined by the lateral dimension a = 310 nm. (b) and (c) show the E_z field profiles for antisymmetric and symmetric mode. (d) compares the magnitude of the attractive optical force for the antisymmetric mode in SiC and Au.

Similar to the simulation for the slab waveguides, we again calculate the optical forces for a range of operating wavelengths that correspond to the same $\mathrm{Re}\{\varepsilon_r(\omega)\}$ for SiC and Au. Figure 6(d) shows the resulting optical forces for the antisymmetric mode. As compared with the SPP optical forces in Au at λ_0 = 543 and 637 nm, the SPhP optical forces in SiC at 11.12 and 11.5 μm are enhanced by a factor of 20. Based on the magnitude of this enhancement, it is likely that its origin stems from a wavelength scale enhancement similar to the one derived

#187913 - $15.00 USD Received 26 Jun 2013; revised 15 Aug 2013; accepted 16 Aug 2013; published 30 Aug 2013

analytically for the slab case in Section 2.2. Given the additional geometric complexity of the modes in this structure though, we are unable to provide a similar closed form approximation.

Such SPhP waveguides provide both stronger optical forces and lower optical losses than plasmonic waveguides. Similar to recent works on hybrid plasmonic waveguides [20, 48, 49], one could envision creating a hybrid phonon-polariton waveguide by combining a polar solid (e.g. SiC) with a nonpolar dielectric. Note that such hybrid waveguides could combine the advantages of low-loss photonic waveguides with strong confinement polariton waveguides, and thus, could help tailor a tradeoff between losses and force enhancement. Nevertheless, due to the material and wavelength advantages highlighted in this work, SPhPs by themselves already provide significant improvements in terms of both enhanced optical forces and reduced losses. More importantly, SPhPs can help expand optomechanical systems to new materials, such as SiC which present superior mechanical properties to the metals used in plasmonic and hybrid plasmonic waveguides.

3. Conclusions

We have investigated the SPhP enhanced optical forces in three different geometries of SiC nanostructures and compared them to the SPP enhanced forces in identical Au nanostructures. For spherical particle dimers in the quasistatic approximation, we isolated the effect of complex permittivity and demonstrated that the near resonance optical forces in SiC around 11 μm wavelengths can be 2 orders of magnitude larger than those for Au at visible wavelengths. For parallel slab waveguides, we demonstrated that, even off resonance (i.e. $\mathrm{Re}\{\varepsilon_r(\omega)\} = -5$ and -10), the optical forces in SiC are still 20 times larger than those calculated for Au. Furthermore, we analytically showed that the optical force is roughly proportional to the operating wavelength under relevant conditions and, therefore, related the 20 fold enhancement factor to the 20 fold increase in operating wavelength from ~500 nm for Au to ~10 μm for SiC. Similarly, in the more practical case of two rectangular waveguides, our simulations again showed that the optical forces in SiC could be enhanced by a factor of 20 as compared to the optical forces in Au. Note that the specific operating wavelengths considered in this paper (e.g., 10.7 μm and 11.1 μm) can be readily accessed using tunable carbon dioxide isotope ($^{13}CO_2$) lasers. Combined with the unique mechanical properties of SiC, especially its high stiffness, these results suggest that the enhanced SPhP forces make SiC a very promising material for infrared optomechanical devices.

Acknowledgments

The authors thank S. Cueff, C.M. Dodson, M. Jiang, S. Karaveli, and J. A. Kurvits for fruitful discussions. This work was supported by the Air Force Office of Scientific Research (PECASE award FA-9550-10-1-0026), the National Science Foundation (CAREER award EECS-0846466, MRSEC award DMR-0520651), and a Richard B. Salomon Faculty Research Award from Brown University.